

Single-Atom Pt Stabilized on One-Dimensional Nanostructure Support via Carbon Nitride/SnO₂ Heterojunction Trapping

Hamin Shin, Wan-Gil Jung, Dong-Ha Kim, Ji-Soo Jang, Yoon Hwa Kim, Won-Tae Koo, Jaehyeong Bae, Chungseong Park, Su-Ho Cho, Bong Joong Kim, and Il-Doo Kim*



Cite This: *ACS Nano* 2020, 14, 11394–11405



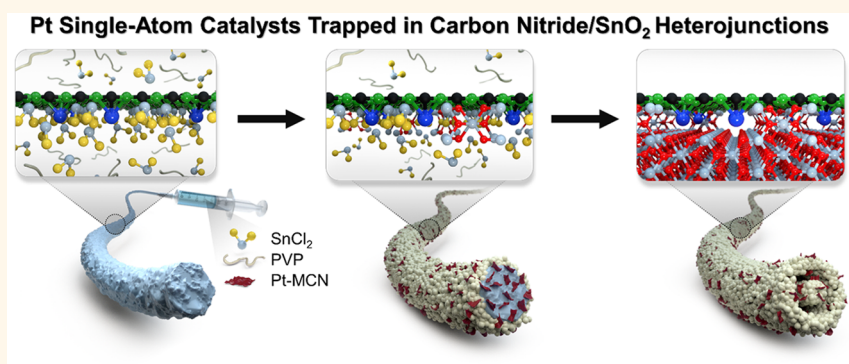
Read Online

ACCESS |

Metrics & More

Article Recommendations

Supporting Information



ABSTRACT: Catalysis with single-atom catalysts (SACs) exhibits outstanding reactivity and selectivity. However, fabrication of supports for the single atoms with structural versatility remains a challenge to be overcome, for further steps toward catalytic activity augmentation. Here, we demonstrate an effective synthetic approach for a Pt SAC stabilized on a controllable one-dimensional (1D) metal oxide nano-heterostructure support, by trapping the single atoms at heterojunctions of a carbon nitride/SnO₂ heterostructure. With the ultrahigh specific surface area ($54.29 \text{ m}^2 \text{ g}^{-1}$) of the nanostructure, we obtained maximized catalytic active sites, as well as further catalytic enhancement achieved with the heterojunction between carbon nitride and SnO₂. X-ray absorption fine structure analysis and HAADF-STEM analysis reveal a homogeneous atomic dispersion of Pt species between carbon nitride and SnO₂ nanograins. This Pt SAC system with the 1D nano-heterostructure support exhibits high sensitivity and selectivity toward detection of formaldehyde gas among state-of-the-art gas sensors. Further *ex situ* TEM analysis confirms excellent thermal stability and sinter resistance of the heterojunction-immobilized Pt single atoms.

KEYWORDS: single-atom catalysts, one-dimensional nanostructure, heterostructure, carbon nitride, metal oxides, gas sensor

For ultimate utilization and efficiency of catalysts, downsizing the catalyst to single atoms (SAs) is essential. Single-atom catalysts (SACs) provide maximum atom utilization efficiency as compared to metal nanoparticles, which are aggregates of hundreds or more atoms, hence limiting the number of metal atoms exposed to the reactants.¹ In pursuit of exploiting the merits of both homo- and heterogeneous catalysis, the SAC must be strongly anchored on a support material to prevent (1) detachment from the support and (2) agglomeration into clusters, during repeated catalytic reactions. Among various types of support materials such as graphene derivatives,^{2–6} carbon-based nanostructures,^{7,8} or other metals,^{9–14} metal oxide supports receive particular interest due to their advantages over other supports in stabilizing SA, as well

as their outstanding stability and performance in multifarious applications.^{14–17}

Since the first SAC system in 2011,¹⁹ several approaches have been implemented to synthesize SACs on oxide supports.^{17,18,20–25} Studies on these systems have reported markedly enhanced catalytic activities including reduced

Received: May 3, 2020

Accepted: August 24, 2020

Published: August 24, 2020



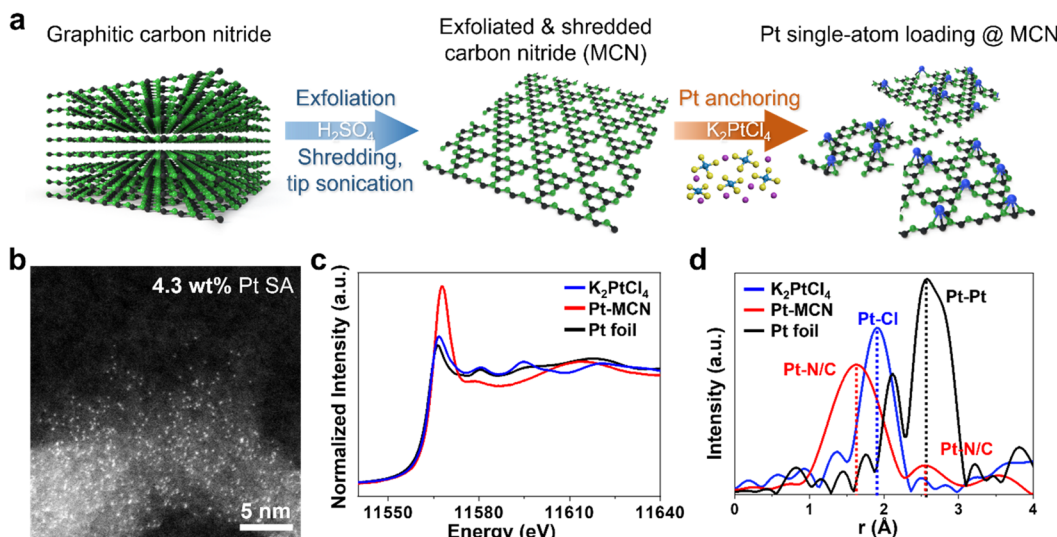


Figure 1. (a) Schematic illustration for the synthesis of Pt SA-anchored shredded carbon nitride nanosheets (Pt-MCNs). (b) HAADF-STEM image of Pt-MCNs with 4.3 wt % Pt SAs. (c) Pt L₃-edge XANES spectra of a Pt-MCN with its references. (d) Fourier transformed (FT) k^2 -weighted $\chi(k)$ -function of the EXAFS spectra for the Pt L₃-edge.

operation temperature,¹⁷ which can be attributed to the maximum catalyst atom utilization efficiency, in addition to increased selectivity.²⁶ Nonetheless, the reported approaches focus mainly on SAC functionalization of bulky metal oxide structures, *i.e.*, thin films and powders, which have a relatively small number of total active sites of the catalytic system itself, and also prevent full exposure of SA on the metal oxide supports. Employing nanostructure-engineered metal oxides as supports for SAC, accordingly, is highly desired to increase the effectiveness of the SAC systems, as numerous studies on supported catalysts have already shown.^{27–29} Despite the benefits, attempts to manipulate the support in nanometer scale are hardly found, which is primarily due to the absence of suitable large-scale synthetic procedures for the fabrication of reliable SAC systems with uniform distribution of SAs throughout the nanofeatures of the metal oxide supports^{1,17,19,30–32} (solution-mediated or vacuum-assisted). There is therefore a crucial need to develop a simple and robust strategy for SACs on nanostructured supports that allows maximization of catalytic activity, precise control of catalyst loading amount, and stable operation over long catalytic cycles.

Recently, graphitic carbon nitride (g-CN), which consists of stacked layers of two-dimensional planes with tris-*s*-triazine repeating units, has been introduced as an effective support for noble metal SAs.^{4–6} The N/C-coordinating framework acts as excellent binding sites for the metal atoms, and these single atoms bound on g-CN show excellent stability throughout repeated catalytic reactions. In addition, the g-CN also shows a high thermal stability,³³ which can effectively prevent the aggregation of SAs under high temperature and at the same time makes g-CN highly compatible to form heterostructures with metal oxides.^{34–37} Hence, g-CN is the most suitable candidate to deliver SACs to metal oxides, which often require high-temperature calcination to oxidize metal precursors.

Herein, we introduce a strategy for stabilizing Pt SA on a metal oxide support with controllable one-dimensional (1D) nano-heterostructures. Pt SA-anchored carbon nitride nanosheets are incorporated in a Sn precursor-containing 1D nanofiber structure *via* electrospinning, and subsequent

calcination results in multi-heterointerface-engineered structures between Pt SA, carbon nitride, and SnO₂. The Pt SAs are strongly immobilized at the heterojunction between carbon nitride and metal oxide, and the system can benefit from the synergistic catalytic enhancement of the Pt SA and the abundant heterojunctions between carbon nitride and SnO₂. High-angle annular dark-field scanning transmission microscopy (HAADF-STEM) and X-ray absorption fine structure spectroscopy (XAFS) reveal successful entrapment of Pt as an SA at the carbon nitride/SnO₂ heterointerface. The SAC system with a nano-heterostructure support exhibits not only excellent catalytic performance in chemiresistive formaldehyde gas detection (response = 33.9 at 5 ppm) but also high thermal stability (7.1% degradation in sensing performance after >170 h of operation at 275 °C) and sinter resistance.

RESULTS AND DISCUSSION

Figure 1a summarizes the synthesis procedure for Pt SA-anchored shredded melamine-derived carbon nitride nanosheets (MCNs), with each MCN having a maximum lateral size of <100 nm. First, during exfoliation, H₂SO₄ is intercalated between the interlayers of graphitic carbon nitride, causing expansion of the interlayer distance.³⁸ Sonication is introduced to exfoliate the g-CN layer by layer. The X-ray diffraction (XRD) (*Supplementary Figure 1*) peak of carbon nitride at 27.4° is related to the stacking of carbon nitride interlayers, and significant reduction and broadening of this peak indicate less of the stacked structure, *i.e.*, exfoliation of g-CN. Exfoliated carbon nitride observed by TEM (*Supplementary Figure 2a*) shows a very thin nanosheet-like structure in contrast to the bulky stacked layer form of g-CN (*Supplementary Figure 2b*). Successive powerful tip sonication applies a large energy on the exfoliated carbon nitride nanosheets, which further downsizes the nanosheets laterally, from a few microns (*Supplementary Figure 3a*) down to less than 100 nm (*Supplementary Figure 3b*).

The purpose of downsizing the g-CN was to increase the exposed binding sites that can anchor the Pt SAs. There have been several attempts to produce Pt SAs on carbon nitride; however, the highest achieved loading was only 0.5 wt %, and a

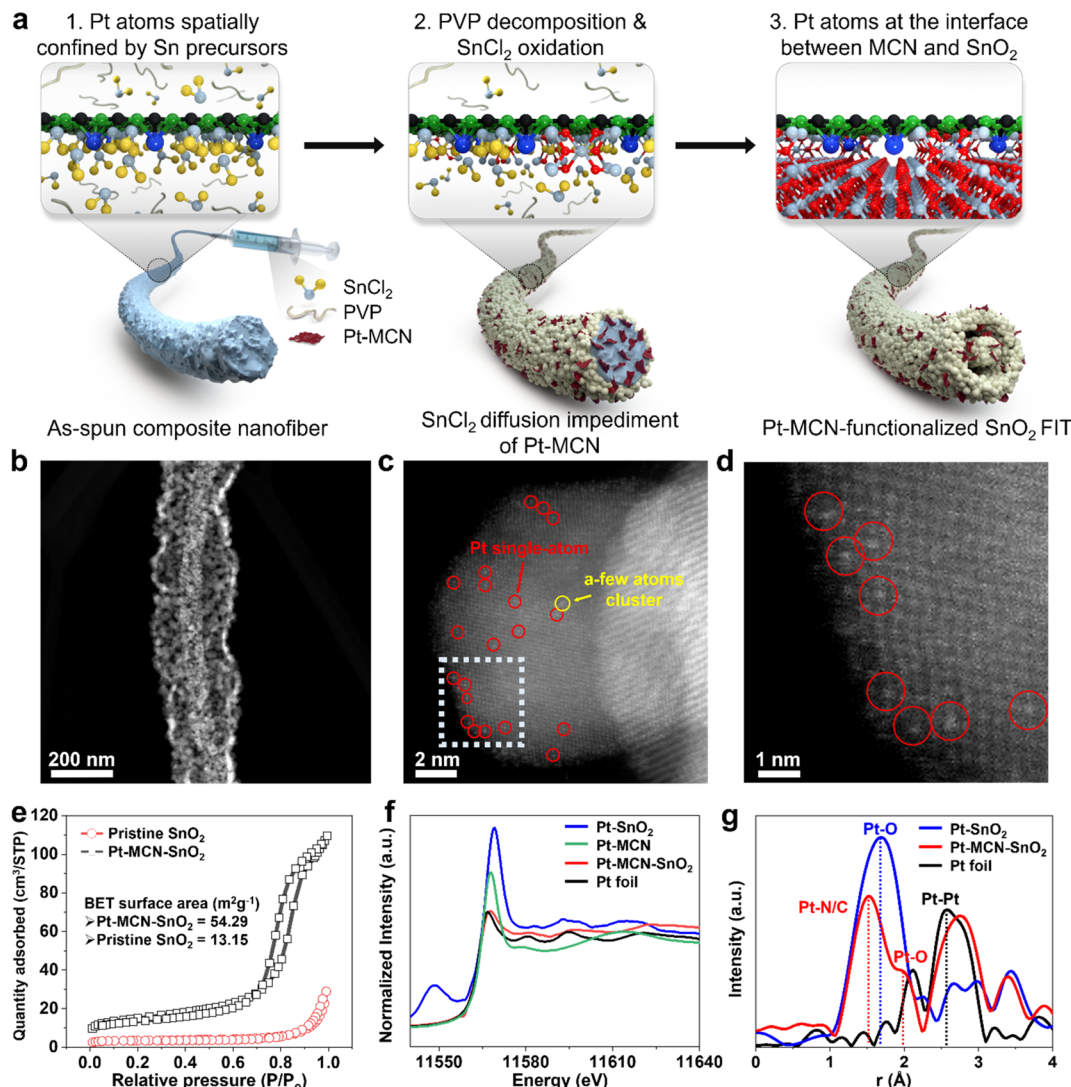


Figure 2. (a) Schematic illustration of the Pt SA delivery process and nanofiber-in-tube (FIT) structure formation. (b) Dark-field STEM image of Pt-MCN-functionalized SnO_2 FIT (Pt-MCN-SnO₂). (c) HAADF-STEM image of Pt-MCN-SnO₂. (d) Magnified image of the white-dotted region in Figure 3c. (e) Brunauer–Emmett–Teller surface area analysis comparison between pristine SnO_2 and Pt-MCN-SnO₂. (f) Pt L₃-edge XANES spectra of Pt-MCN-SnO₂ with its references. (g) Fourier-transformed (FT) k^2 -weighted $\chi(k)$ -function of the EXAFS spectra for the Pt L₃-edge.

slight increase in the Pt loading resulted in the formation of a vast proportion of Pt clusters.^{4,5,39} The same Pt SA anchoring process was carried out for MCNs with significantly increased surface area, using wet impregnation. The inductively coupled plasma optical emission spectrometry (ICP-OES) analysis suggested that the Pt content on Pt-MCNs is as high as 4.3 wt %, which is the highest Pt SA loading ever achieved on carbon nitride. Figure 1b is a clear display of the uniform distribution of atomic-sized Pt all over the surface of the MCN, which can be identified by the bright spots among the gray area that corresponds to the MCN. To more evidently verify the uniform atomic dispersion of Pt, X-ray photoelectron spectroscopy (XPS) and X-ray absorption spectroscopy (XAS), which includes X-ray absorption near edge structure (XANES) and extended X-ray absorption fine structure (EXAFS) analysis, were conducted.

The Pt 4f spectra (Supplementary Figure 4a) of the Pt-MCN shows that Pt atoms on the Pt-MCN are in an oxidized state with a binding energy of Pt 4f_{7/2} at 72.8 eV and Pt 4f_{5/2} at 76.10 eV, which is close to the binding energy of Pt²⁺, yet

slightly higher than the reported binding energies of typical Pt²⁺ oxidation states from XPS.^{40,41} This result suggests that the Pt coordinated with five N/C⁵ has caused the Pt atoms to have a slightly more positively charged valence state than those Pt species of the conventional Pt nanoparticles with Pt–O bonds. Moreover, the N 1s spectra (Supplementary Figure 4b) of the Pt-MCN shows that the peak has been slightly shifted to a lower binding energy compared to that of MCN (Supplementary Figure 4c), which can be attributed to the withdrawal of electrons from Pt SA toward highly electronegative N.

The normalized XANES spectra (Figure 1c) for the Pt-MCN in comparison with the Pt foil and K₂PtCl₄ is consistent with the XPS data, which show that the Pt atoms in Pt-MCN are in oxidized states with Pt^{δ+} valence (+2 < δ) as compared to the metallic Pt and Pt²⁺ (for magnified XANES spectra, see Supplementary Figure 5). In addition, the Pt-MCN shows a higher Pt white line intensity relative to that of K₂PtCl₄ as well as a slight increase in the energy, indicating a higher oxidation state of Pt of Pt-MCN in comparison to its precursor.^{42,43} The

Fourier transform (FT)-EXAFS of Pt-MCN (Figure 1d) was conducted to investigate the neighboring atoms of Pt. A sharp dominant peak with a total Gaussian distribution at $\sim 1.61 \text{ \AA}$ corresponds to the Pt–N/C bond in direct coordination with the Pt SA, and the second dominant peak at $\sim 2.8 \text{ \AA}$ corresponds to the second nearest N/C. Note that the Pt–N and Pt–C bonds are very difficult to distinguish using EXAFS, due to their similar scattering parameters originating from their neighboring positions on the periodic table.⁵ In addition, there is no noticeable peak that corresponds to the Pt–Pt bond for the Pt-MCN, indicating that the majority of Pt species on the MCN are in an atomically dispersed state. EXAFS curve-fitting (fitting parameters are given in Supplementary Table 1) was carried out for the Pt-MCN using previously reported models for graphitic carbon nitride,³⁹ to obtain the first-shell and second-shell distances and corresponding coordination numbers of Pt (Supplementary Figure 6). There are Pt–N/C contributions at 1.96 \AA for the first shell and 2.43 \AA for the second shell. Summing up the results obtained using the HAADF-STEM, XPS, and XAS, we conclude that Pt is well dispersed atomically on the MCN.

The as-synthesized Pt SA anchored on melamine-derived carbon nitride (Pt-MCN) was then simply mixed with a typical electrospinning solution, which consists of a metal precursor, a high molecular weight polymer, and a solvent to dissolve all solutes. After being stirred at room temperature, the solution is electrospun into a nanofiber (NF) mat and calcined at a temperature high enough to completely oxidize the metal precursor and remove all of the polymer matrix within the as-spun NFs. We chose melamine over several other precursors to synthesize g-CN because of its large molecule size. The large molecule size of melamine allows the formation of highly crystalline g-CN^{33,42–51} with high thermal stability. The g-CN derived from melamine shows thermal stability up to temperatures $>550 \text{ }^{\circ}\text{C}$ (Supplementary Figure 7a), and the excellent thermal stability is retained even after the exfoliation, tip sonication, and Pt wet impregnation processes (Supplementary Figure 7b). The minor decrease in the weight at temperatures below $550 \text{ }^{\circ}\text{C}$ can be attributed to evaporation of ethanol that remained after the washing and drying steps. For this reason, the calcination temperature for the electrospun NFs was deliberately set to $500 \text{ }^{\circ}\text{C}$, which is the temperature that is sufficiently high to form metal oxide NFs and, at the same time, allows the Pt-MCN to remain inside the NF structure after the calcination process.

Incorporation of large foreign particles or large organic molecules inside the NF structures causes formation of nanofiber-in-tube (FIT) structures after calcination processes.^{52,53} One can expect the addition of a Pt-MCN to the electrospun NFs to exhibit a similar phenomenon. Figure 2a illustrates the synthesis procedure of a Pt-MCN-functionalized tin oxide (SnO_2) FIT structure (hereafter, Pt-MCN- SnO_2). When the electrospinning solution containing Pt-MCNs is electrospun, the Pt-MCNs are very uniformly dispersed throughout; however, occasionally some relatively large or aggregated Pt-MCNs within the as-spun nanofibers can be directly observed by SEM (Supplementary Figure 8a). In comparison, the as-spun nanofibers without Pt-MCN addition show a very smooth surface morphology (Supplementary Figure 8b). The formation mechanism of the FIT structure during the calcination is summarized in Supplementary Figure 9. The FIT structure was confirmed using STEM analysis in Figure 2b, where the contrast in the brightness shows that an

NF with a diameter of roughly 70 nm is inside a nanotube with a larger diameter ($\sim 250 \text{ nm}$). The dark-field (DF) STEM image of the FIT in Figure 2b shows a very rough surface morphology of the exterior nanotube, which can be attributed to the Pt-MCNs that reside uniformly within the FIT structure. Note that 2D nanosheets readily transform into crumpled morphologies upon high-voltage electrospinning.^{54,55} Pt-MCNs possess highly δ^- surface charge characteristics that can bind Sn^{2+} ions onto its surface; hence, after calcination, the surface morphology of the nanotubes is highly roughened by the oxidation of Sn^{2+} ions attached on the crumpled Pt-MCNs. The FIT structure becomes more defined as the Pt-MCN content is increased (Supplementary Figure 10 a–e). The advantage of having the FIT structure is that both the interior and the exterior surfaces of the nanotube, as well as the NF inside the nanotube, can provide much increased catalytic reaction sites, therefore showing higher catalytic performance than that of dense NFs.^{52,53} The pore size distribution of Pt-MCN- SnO_2 (Supplementary Figure 11) shows a tremendously increased number of mesopores in the size range between 5 and 20 nm compared to the dense pristine SnO_2 NF. This gave rise to the markedly increased surface area of $54.29 \text{ m}^2 \text{ g}^{-1}$ for Pt-MCN- SnO_2 according to the Brunauer–Emmett–Teller (BET) surface area analysis, compared to that of the pristine SnO_2 NF ($13.15 \text{ m}^2 \text{ g}^{-1}$) (Figure 2e). XRD analysis results (Supplementary Figure 12) of the pristine SnO_2 NF and the Pt-MCN- SnO_2 FITs reveal that addition of Pt-MCNs does not alter the crystal structure of SnO_2 ; however, from the calculation of the average grain size by the Scherrer equation (for further information, see the Supporting Information), we could observe that the average grain sizes of the pristine SnO_2 NFs and Pt-MCN- SnO_2 FITs are 10.57 and 8.47 nm , respectively. The reduction in the average grain size in Pt-MCN- SnO_2 is attributed to the restrained SnO_2 grain growth by the Pt-MCNs, and a similar phenomenon has been reported in many previous research.^{56–58}

Figure 2a additionally illustrates the delivery of Pt SA to the Pt-MCN- SnO_2 . The δ^- surface charges of Pt-MCNs are ideal adsorption sites for Sn precursors, and we believe that the uniformly adsorbed thin layer of Sn precursors on Pt-MCN would spatially confine and immobilize the Pt SAs on Pt-MCNs, hence preventing agglomeration during the calcination.¹⁸ The physical states of Pt SAs on Pt-MCNs after electrospinning and subsequent calcination processes were investigated with HAADF-STEM analysis (Figure 2c and d). The atomic number difference between Pt ($Z = 78$) and Sn ($Z = 50$) is not as large as that between Pt and C ($Z = 6$) and N ($Z = 7$); however, the Pt species were still clearly visible by their z-contrast with Sn. The STEM image shows bright spots on top of SnO_2 grains that are mismatched with the SnO_2 lattice. This clearly reveals that individual Pt atoms are well stabilized on the SnO_2 FITs (red circles), although there seems to exist occasionally a few-Pt-atom clusters (yellow circle).

To further verify whether the Pt atoms from Pt-MCNs are transferred from MCNs onto SnO_2 defect sites or remain strongly trapped between MCNs and SnO_2 , we conducted XAS analysis. The normalized XANES spectra for Pt-MCN- SnO_2 compared with the Pt foil, Pt-MCNs, and Pt-doped SnO_2 (Pt- SnO_2) (Figure 2f) show that Pt species of Pt-MCN- SnO_2 are at an oxidation state between those of metallic Pt and the PtO_x of Pt-doped SnO_2 (for magnified XANES spectra, see Supplementary Figure 13). Pt of Pt- SnO_2 shows a much higher white line intensity and higher peak energy position relative to

that of Pt-MCN-SnO₂. This result indicates that Pt species in Pt-MCN-SnO₂ are to a large degree at a lower oxidation state than that of Pt-SnO₂, hence excluding the possibility of Pt incorporation into Sn⁴⁺ vacancy sites of SnO₂. Pt species of Pt-MCN-SnO₂ and Pt-MCN have almost the exact same peak positions at ~11574 eV; however, a decrease in the white line intensity of Pt species in Pt-MCN-SnO₂ in comparison with those of Pt-MCN indicates a slight reduction of Pt oxidation state during the electrospinning and calcination steps.^{41,42} We hypothesized that this reduction in the oxidation state could have been caused by the electron transfer from Sn in SnO₂ to Pt, due to the differences in the electronegativity (Sn: 1.96, Pt: 2.28). FT-EXAFS of Pt-MCN-SnO₂ (Figure 2g) shows the second most dominant peak of the Pt-MCN is the peak centered at 2.76 Å. This peak could have been contributed by three candidates, which are Pt–Sn, Pt–Pt from possible Pt nanoparticle formation *via* sintering of Pt SA, and the second nearest Pt–N/C that was observed also in Figure 1d. Formation of a bimetallic bond is already reported in previous literature with metal-oxide-based single-atom structure.¹⁹ The EXAFS fitting was carried out using the graphitic carbon nitride model and a SnO₂ tetragonal crystal model (for details, see Supplementary Figure 14 and Supplementary Table 1). The fit for the first shell (Pt–N/C) gives the coordination number (CN) of 5 and the distance (*R*) of 1.6 Å. This result suggests that Pt single atoms are not detached from the MCN and still remain firmly stabilized even after the heat treatment. For the second-shell fitting, the CN is 1.9 and the *R* is 1.99 Å, which is consistent with what was reported in Pt SAs stabilized on FeOx.¹⁹ The result suggests that the Pt SAs in Pt-MCN-SnO₂ are not just stabilized by MCNs but trapped at the heterojunction between MCNs and SnO₂ nanograins and emphasizes the possibility that the peak centered at 2.76 Å has a large Pt–Sn contribution. The existence of the Pt–Sn bond supports our hypothesis that the electron transfer from Sn of SnO₂ to Pt causes the reduction in the oxidation state of Pt in Pt-MCN-SnO₂; Pt still remains firmly anchored on MCNs, but the electrons transferred from Sn reduce the Pt species and make them almost metallic. The Pt 4f XPS spectrum of Pt-MCN-SnO₂ (Supplementary Figure 15) agrees with the XANES data, since the major binding energy peaks correspond to Pt^{δ+} at 71.96 eV for 4f_{7/2} and 74.98 eV for 4f_{5/2}, which are at a significantly reduced state relative to those of Pt-MCNs (Supplementary Figure 16) (Pt 4f_{7/2} at 72.8 eV and Pt 4f_{5/2} at 76.10 eV), yet still at a higher oxidation state than those of Pt nanoparticles (Pt 4f_{7/2} at 71.2 eV and Pt 4f_{5/2} at 74.7),⁵⁸ indicating that agglomeration of Pt is unlikely to have occurred. The largest peak at around 1.53 Å corresponds to Pt–N/C, which is clearly different from that of Pt–O of PtO₂ at 1.68 Å. This peak first demonstrates that the MCN still remains inside the Pt-MCN-SnO₂ after the calcination and also that the Pt species are still strongly anchored on the MCN. The existence of Pt-MCNs after the calcination process is also indirectly demonstrated by the N 1s XPS spectra of Pt-MCN-SnO₂ (Supplementary Figure 17). The EXAFS analysis supports the enhanced stability of Pt SA anchored on the Pt-MCN under the high-temperature annealing process, in agreement with the HAADF images of Pt-MCN-SnO₂. From the STEM and EXAFS results, we conclude that the Pt SAs of Pt-MCNs are not aggregated even through harsh synthesis conditions and are trapped at the heterojunctions of the MCN/SnO₂ heterostructure. Hence, the Pt SAs on Pt-MCN-SnO₂ can be thought to be stabilized by both MCN and SnO₂,

and one can expect the Pt SAs to show highly stable catalytic performance.

The Pt-MCN-SnO₂SAC system, with abundant Pt₁–N/C (isolated Pt bonded with N and C) on a 1D nano-heterostructure metal oxide support, has outstanding potential to be employed in various catalytic reactions, especially due to the synergistic catalyst effect of the Pt SAs and the heterojunctions between MCNs and SnO₂. To demonstrate the superiority of Pt-MCN-SnO₂ in terms of catalysis, it was applied as a catalyzed chemiresistive gas-sensing system. Metal oxide gas sensors often require high-temperature operation (>250 °C); therefore, it is the most suitable application to demonstrate the superior stability of Pt-MCN-SnO₂. One issue that can be addressed when employing Pt-MCN-SnO₂ as a gas-sensing layer is the accessibility of target gas molecules to the trapped Pt SAs at the heterojunction. An interesting characteristic of carbon nitride is that it possesses abundant micropores (1–2 nm) in its planar structure.⁴⁷ These micropores, so-called “nitrogen pots”, act as excellent stabilization sites for various single transition metal atoms and, at the same time, can work as access channels for the target gas species that are introduced to the Pt-MCN-SnO₂ system. Since the kinetic diameters of most gas species that are targeted for gas sensing or catalytic conversion are less than 1 nm (for example, acetone is 4.6 Å and methanol is 3.6 Å),⁵⁹ the target gas molecules would have no problem passing through the micropores on MCNs and reaching the trapped Pt single atoms. Moreover, it is very unlikely that the MCNs (~50–100 nm size) are fully covered with SnO₂ nanograins, since the 1D SnO₂ body is highly mesoporous (~12 nm size pores, Supplementary Figure 11). Hence, Pt-MCN-SnO₂ can accommodate gas phase reactions on the Pt single atoms trapped at the heterojunctions.

An alumina substrate used for the chemical gas sensing test is illustrated in detail in Supplementary Figure 18. To be specific, the alumina substrate has interdigitated Au electrodes (25 μm width and 150 μm electrode gap), and it measures the dynamic resistance change of the gas-sensing materials upon exposure to different concentrations of formaldehyde gas.

Prepared gas sensor samples were tested with formaldehyde gas at different concentrations varying from 5 to 0.05 ppm (50 ppb) at 275 °C, which was the optimum operation temperature for all Pt-MCN-SnO₂ sensor samples (Supplementary Figure 19). Relative humidity (RH) was kept at ~5%, to exclude the interference of water molecules on formaldehyde gas and the sensor materials. The Pt-MCN content optimization was also carried out at 275 °C (Supplementary Figure 20).

The sensing performance of the optimized Pt-MCN-SnO₂ sample was investigated in comparison with those of Pt-doped SnO₂ NFs (Pt-SnO₂), MCN-SnO₂ FITs without Pt catalyst, and pristine SnO₂ NFs. Addition of Pt precursors to the electrospinning solution allows uniform mixing of Pt precursors and Sn precursors, hence, after calcination, forms a SnO₂ structure with uniformly doped Pt, which almost mimics the singly isolated Pt system without an additional support like the Pt-MCNs.⁵⁷ XPS analysis of Pt-SnO₂ (Supplementary Figure 21) shows the Pt⁴⁺ oxidation state,⁶⁰ which verifies that Pt is well dispersed within the SnO₂ lattice. Pt-SnO₂ and MCN-SnO₂ show 2.2 times (*R*_{air}/*R*_{gas} = 17.0 at 5 ppm) and 1.4 times (*R*_{air}/*R*_{gas} = 10.8 at 5 ppm) higher responses than that of pristine SnO₂, respectively, toward formaldehyde throughout the whole concentration range (Figure 3a). The enhancement in sensing property for Pt-

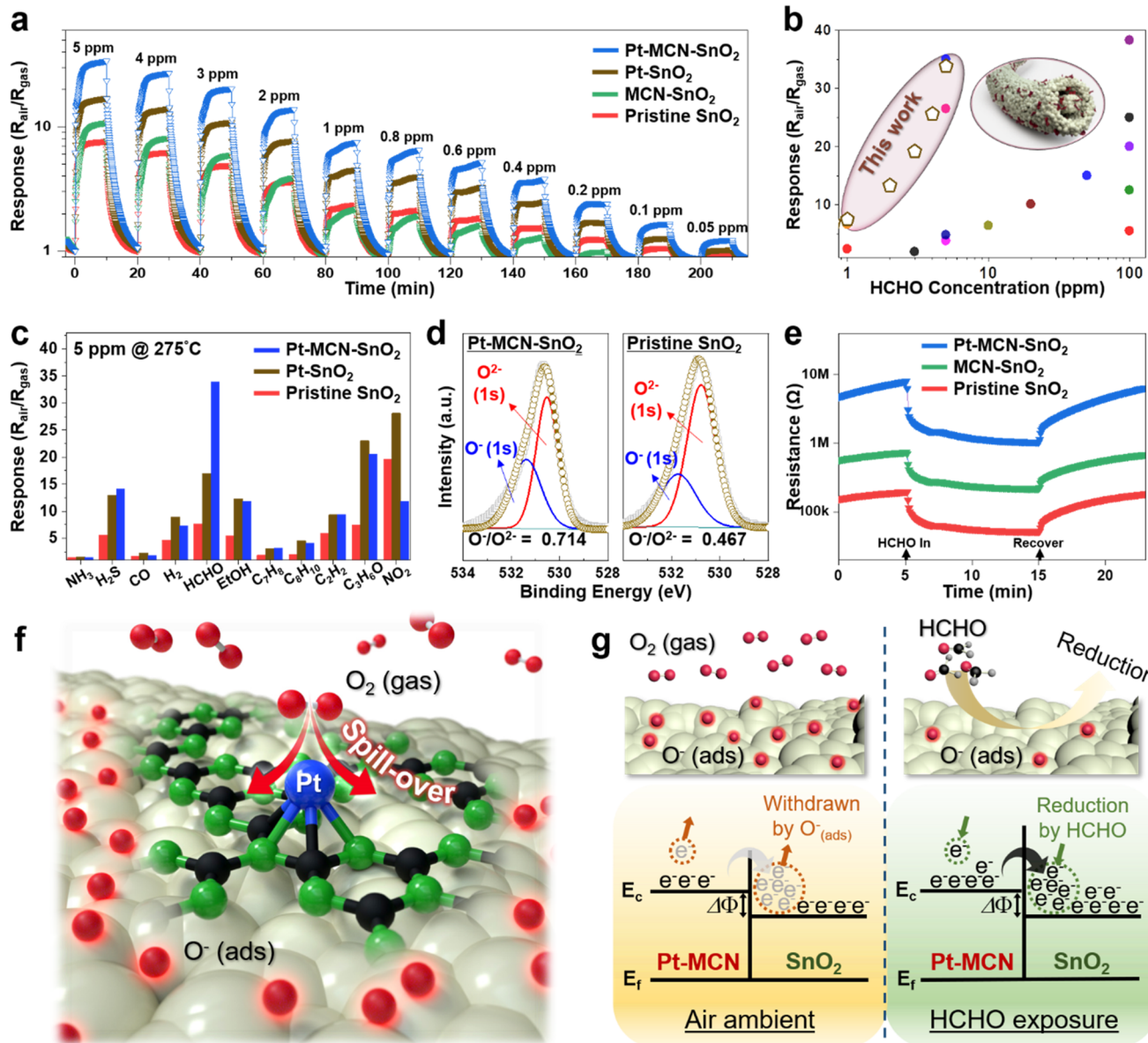


Figure 3. (a) Formaldehyde gas sensing results of Pt-MCN-SnO₂ compared with reference samples. (b) Response values of state-of-the-art formaldehyde gas sensors compared with that of Pt-MCN-SnO₂. (c) Selectivity of Pt-MCN-SnO₂ toward nine different gas species compared with reference samples. (d) XPS spectra of Pt-MCN-SnO₂ and pristine SnO₂ in the vicinity of O 1s. (e) Dynamic resistance transition of pristine SnO₂, MCN-SnO₂, and Pt-MCN-SnO₂ under 1 ppm formaldehyde exposure and recovery. (f) Schematic illustration of O₂ (gas) dissociation over Pt SAs on Pt-MCN-SnO₂ and chemisorbed oxygen species (O⁻ (ads)). (g) Schematic illustration of the HCHO-sensing mechanism and simplified energy band diagram of the heterojunction between MCN and SnO₂. Withdrawal and retrieval of electrons at the electron accumulation layer cause larger variations of resistance.

SnO₂ can be attributed to the well-known catalytic effects of Pt doping for Pt-SnO₂,^{61,62} and the enhancement in sensing property in MCN-SnO₂ proves the catalytic effect of the heterojunction formed between MCNs and SnO₂ (for a detailed explanation regarding the sudden decrease in response value of MCN-SnO₂, see *Supplementary Figure 22*). However, it is clearly demonstrated that Pt-MCN-SnO₂ shows a far superior gas-sensing performance ($R_{\text{air}}/R_{\text{gas}} = 33.9$ at 5 ppm) compared to those of both Pt-SnO₂ and MCN-SnO₂. The further enhancement in the response toward formaldehyde would have originated from the synergistic influences of maximized catalyst atom efficiency by atomic isolation of Pt and the heterojunction effect and the morphological control caused by MCN.⁶³ In fact, Pt-MCN-SnO₂ shows the first-

ranked sensing performance toward formaldehyde gas over other state-of-the-art formaldehyde gas sensors (Figure 3b). A detailed comparison of sensing properties of the state-of-the-art HCHO gas sensors is summarized in *Supplementary Table 2*. This is a surprisingly outstanding result, and we believe that further careful optimization would readily allow us to attain the most effective catalytic system for gas sensors. Furthermore, combining SACs and metal oxide supports of different elements may allow us to build a library of gas sensors with different selectivity, similar to what is shown in the previous literature of nanoparticle-based gas sensor systems.⁵⁷

For further assessment of the catalytic performance of the designed SAC system, we investigated the catalytic effects of Pt₁-N/C and the heterostructure on the selectivity of gas

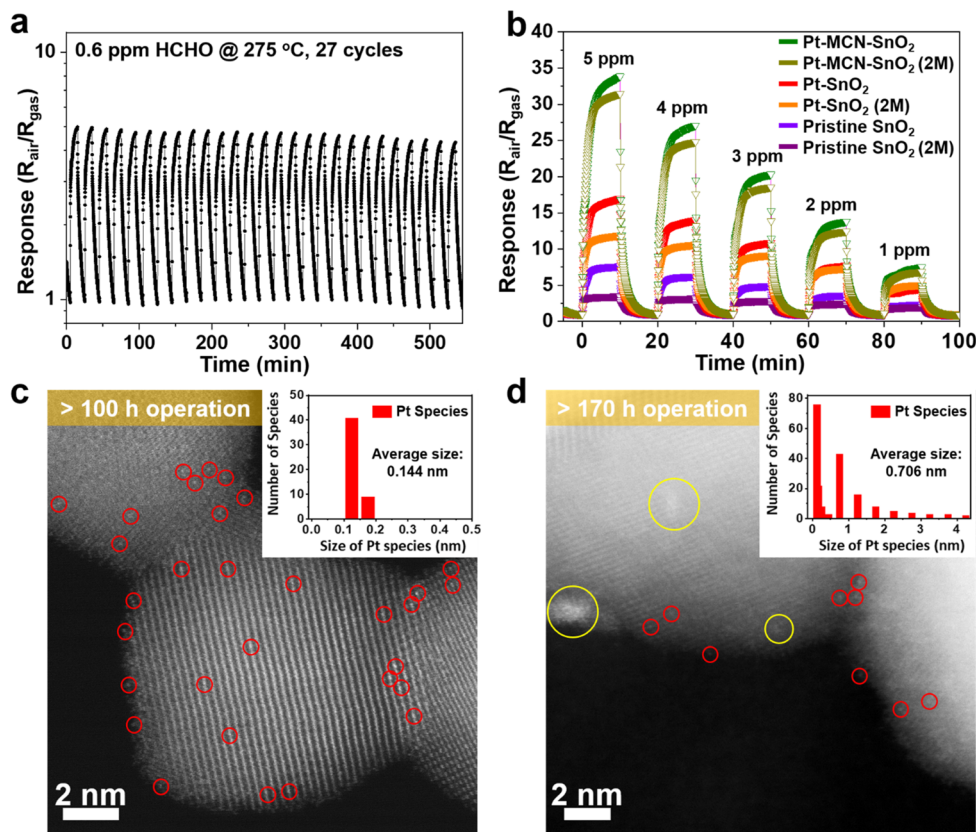


Figure 4. (a) Cyclic stability of Pt-MCN-SnO₂ through 27 cycles of 0.6 ppm of HCHO exposure. (b) Long-term stability of Pt-MCN-SnO₂ in comparison with reference samples; 2 M represents that the sample has been re-evaluated after 2 months storage on a shelf under an air atmosphere. (c) HAADF-STEM image of a >100 h postoperation Pt-MCN-SnO₂ sample (inset is Pt size distribution). (d) HAADF-STEM image of a >170 h postoperation Pt-MCN-SnO₂ sample (inset is Pt size distribution).

sensors by comparing with pristine SnO₂ NFs and Pt-SnO₂ NFs. The responses of Pt-MCN-SnO₂, Pt-SnO₂, and pristine SnO₂ toward 10 different gas species that commonly exist in air were measured (Figure 3c), which are ammonia (NH₃), hydrogen sulfide (H₂S), carbon monoxide (CO), hydrogen (H₂), ethanol (EtOH), toluene (C₇H₈), xylene (C₈H₁₀), acetylene (C₂H₂), acetone (C₃H₆O), nitrogen dioxide (NO₂), and formaldehyde (HCHO). Enhancement in the sensitivities toward almost all gases is apparent for both Pt-SnO₂ and Pt-MCN-SnO₂. SnO₂-based chemiresistive gas sensors tend to show very high responses toward several different gases, namely, H₂S, HCHO, EtOH, and C₃H₆O, and their selectivity can be enhanced by employing noble metal catalysts.^{56,58} Pt doping in SnO₂ often shows an enhanced sensitivity toward acetone, and the same phenomenon was observed from the selectivity test results in Figure 3c. In contrast, Pt-MCN-SnO₂ exhibits largely enhanced selectivity toward formaldehyde, while having similar sensitivity toward H₂S, EtOH, and acetone compared to those of Pt-SnO₂. This is an indication that Pt₁-N/C could have a catalytic mechanism that either strengthens the adsorption of HCHO molecules by acting as binding sites for HCHO or promotes easier dissociation of HCHO gas to react with the chemisorbed oxygen species (O[−]_(ads)) on the tin oxide body. We also carried out further gas-sensing evaluation on Pt-MCN-SnO₂ to observe the humidity effect on the response toward formaldehyde gas (for details, Supplementary Figure 23).

XPS analysis (Figure 3d) reveals an increase in the ratio between O[−] (chemisorbed oxygen species) and O^{2−} (lattice

oxygen species) for Pt-MCN-SnO₂ (O[−]/O^{2−} = 71.4%) over that of pristine SnO₂ (O[−]/O^{2−} = 46.7%). This is a direct indication of the increased number of chemisorbed oxygen species on the surface of Pt-MCN-SnO₂ in comparison to pristine SnO₂. An increase in the chemisorbed oxygen species is well known to thicken the electron depletion layers of the metal oxide nanograins, hence increasing the baseline resistance of gas sensors.^{53,58} This is also implied by observing dynamic resistance transitions (Figure 3e) of pristine SnO₂, MCN-SnO₂, and Pt-MCN-SnO₂ upon HCHO exposure, where Pt-MCN-SnO₂ (~8 MΩ) shows an almost 40-fold increase in the baseline resistance with respect to that (~0.2 MΩ) of pristine SnO₂. The enhanced oxygen chemisorption can be attributed to two major factors—enhanced spillover effect by Pt–N/C bonding and heterojunction formation between Pt-MCN and SnO₂—and one minor factor: increased surface area due to FIT structure formation. It has been reported that not only the Pt SAs but also the pyridinic nitrogen site can greatly enhance the oxygen spillover.⁶⁴ Specifically, the theoretical studies show that the Pt–N/C site provides a very strong adsorption site for O₂ with the adsorption energy of −1.93 eV, and moreover, the O–O bond length of O₂ adsorbed on the Pt atom is longer than that of O₂ adsorbed on Pt bulk. Such facts promote easier O₂ adsorption and dissociation on Pt SA over to the SnO₂ sensing body, hence increasing the concentration of surface chemisorbed oxygen species (Figure 3f). To demonstrate this suggestion, we carried out further formaldehyde gas sensing evaluation with the same Pt-MCN-SnO₂ sample with the same loading density

of Pt but in nanoparticle form (PtNP-MCN-SnO_2) for comparison (Supplementary Figure 24), so that the Pt nanoparticles are trapped at the heterojunction between MCNs and SnO_2 . PtNP-MCN-SnO_2 indeed shows superior sensitivity toward formaldehyde (response = 25.8) compared to MCN-SnO_2 (response = 15.4) and Pt-SnO_2 (response = 17.0), but not as high as that of Pt-MCN-SnO_2 (response = 33.9) with Pt SAs, which further emphasizes the catalytic effect of Pt–N/C, the maximized catalyst atom efficiency, and the minimum coverage of active sites on SnO_2 . In addition, it is also highly possible that the regions on SnO_2 functionalized with Pt SA promote stronger adsorption of formaldehyde gas onto the sensing body, leading to increased removal of chemisorbed oxygen and increased electron density with respect to bare SnO_2 regions with no Pt functionalization. The difference in the electron density causes further charge transfer between Pt SA-functionalized SnO_2 and bare SnO_2 , which in turn further reduces the overall resistance of the sensing layer upon formaldehyde gas exposure.

Incorporation of Pt-MCN in Pt-MCN-SnO_2 forms the aforementioned heterojunctions between Pt-MCN and SnO_2 . The work function of pristine SnO_2 NFs has been found to be 4.48 eV (Supplementary Figure 25a,b). After the addition of Pt-MCN into SnO_2 , we observed a clear drop in the work function to 4.38 eV (Supplementary Figure 25c,d), which is indicative of electron transfer from Pt-MCN to the SnO_2 main body. This observation suggests the second enhancement mechanism, the heterojunction formation (Figure 3g), in which the electron accumulation layer formed between SnO_2 and MCNs is favored for more adsorption of oxygen species, therefore increasing the concentration of chemisorbed oxygen on the surface of Pt-MCN-SnO_2 .² In addition, the withdrawal and retrieval of electrons at the electron accumulation layer will cause larger variations in the resistance, hence, larger response values. MCN-SnO_2 ($\sim 1 \text{ M}\Omega$) also shows a ~ 5 -fold increase in the baseline resistance relative to that of pristine SnO_2 (Figure 3e), which is an indication of increased chemisorbed oxygen species due to the formation of electron accumulation layers at the heterointerfaces.

One additional fascinating feature obtained from the gas-sensing results was the high stability of Pt SA on Pt-MCN-SnO_2 , which is as we expected when we observed that the Pt SAs are trapped between the heterojunction. The Pt SAs strongly anchored on Pt-MCN have not only survived under the harsh calcination conditions (500 °C for 1 h) for producing the Pt-MCN-SnO_2 FITs but also demonstrate markedly stable catalytic performance for long cyclic operations (Figure 4a). The sensitivity, sensing speed, and recovery time are all well maintained throughout 27 repeated cyclic exposures to HCHO. Moreover, the gas sensor samples exposed to cyclic exposure to HCHO at 275 °C for 1 week (>170 h) were stored on a shelf for 2 months and then reoperated to determine the degree of performance degradation (Figure 4b). Surprisingly, Pt-MCN-SnO_2 shows only 7.1% degradation in the sensor response toward 5 ppm of HCHO, whereas Pt-SnO_2 and pristine SnO_2 show 30.0% and 54.1% degradation in the sensor response toward 5 ppm of HCHO, respectively. This implies that Pt-MCN-SnO_2 is very resistant to degradation even at repeated high-temperature operation and long shelf life.

The superior stability, as discussed, is believed to be attributed to the strong sinter resistance of the Pt SAs entrapped between carbon nitride and SnO_2 . To verify this

hypothesis, we further conducted *ex situ* TEM analysis on Pt-MCN-SnO_2 operated under 275 °C for >100 h and >170 h. HAADF-STEM of Pt-MCN-SnO_2 operated at 275 °C for >100 h (Figure 4c) clearly shows Pt SAs (red circles) remain atomically dispersed, demonstrating Pt SAs on Pt-MCN-SnO_2 are highly resistant toward agglomeration. The particle size distribution (50 e.a., Figure 4c, inset) shows that the average size of Pt is $0.144 \pm 0.011 \text{ nm}$, which is very close to the well-known size of a Pt single atom ($\sim 0.14 \text{ nm}$). After >170 h of operation, the HAADF-STEM image (Figure 4d) reveals that Pt SAs still remain stabilized atomically (red circles); however, clear signs of Pt agglomeration can also be observed (yellow circles). The same is also observed in the high-resolution TEM (HRTEM) image (Supplementary Figure 26), where black spots that are mismatched with the SnO_2 nanograins are visible (SnO_2 confirmed with FFT in inset figure). These atomic clusters might originate from agglomeration of fairly weakly bound Pt SAs that are delocalized from their positions at the heterojunction due to continuous high-temperature operation. Despite the slight agglomeration of Pt, from the size distribution of Pt, we find that there is only a minor increase in the average size of Pt species to $0.706 \pm 0.852 \text{ nm}$ (Figure 4d, inset, 195 e.a.). Such findings are considered to be the origin of excellent long-term thermal stability of Pt-MCN-SnO_2 , far superior to that of Pt-doped SnO_2 with only a 7.1% performance decay after >170 h of high-temperature operation. The excellent stability of Pt SAs in this work compared to many of the previously reported SAC systems is therefore attributed to the dual-stabilization effect from MCNs and the SnO_2 nanograins that confine Pt SAs on Pt-MCNs, which prevents migration of Pt SAs and, as a result, prevents the agglomeration of Pt SAs into clusters. This work suggests an approach to synthesize a SAC system supported by a nano-heterostructure metal oxide, which, in turn, maximizes the total number of active sites on a catalytic system and, at the same time, benefits from additional catalytic enhancement of the heterostructure. We believe that such an approach has the potential to be applied in various fields of catalysis that can be benefitted from reliable metal oxide supports with a large number of active sites and highly stable SACs.

CONCLUSIONS

In summary, we proposed a design principle for a single-atom catalyst system with a 1D SnO_2 nano-heterostructure support using Pt-MCNs and an electrospinning technique. The heterojunction between carbon nitride and SnO_2 not only firmly stabilizes the Pt SAs by spatially confining the SAs but also takes part in the catalyzed surface reaction for formaldehyde detection, which makes the catalytic performance of the SAC system even more effective. The dual-catalytic effects of both Pt SA and the MCN/ SnO_2 heterostructure with high specific surface area allowed us to achieve exceptionally high catalytic performance in its application as chemical gas sensors, showing one of the world's best responses toward formaldehyde gas. Moreover, the Pt SAs immobilized at the heterojunctions possess excellent stability for a nanocatalytic system, showing only a 7.1% degradation even after >170 h of gas-sensing operation at 275 °C. We anticipate that the design principle for these heterojunction-stabilized single-atom catalysts supported by a 1D metal oxide nanostructure will largely extend the options in constructing metal-oxide-based SAC systems and will be applicable to a wide range of catalytic

reactions, especially those that require long cyclic reactions under harsh temperature conditions.

EXPERIMENTAL SECTION

Materials. Polyvinylpyrrolidone (PVP, $M_w \sim 1\,300\,000$ g mol $^{-1}$), melamine (99%), tin(II) chloride dehydrate ($\text{SnCl}_2 \cdot 2\text{H}_2\text{O}$, 98%), *N,N*-dimethylformamide (DMF, 99.8%), sulfuric acid (ACS reagent, 95.0–98.0%), platinum nanoparticle dispersion (3 nm particle size, 1000 ppm in H_2O , 99.99% trace metals basis), and potassium tetrachloroplatinate(II) (K_2PtCl_4) were purchased from Sigma-Aldrich. All materials were used without further purification.

Preparation of Pt-MCN. First, bulk graphitic carbon nitride was synthesized by directly heating melamine. A 10 g amount of melamine was put in a closed alumina crucible and then in a muffle furnace and heated at 550 °C for 3 h under ambient conditions, with a ramping rate of 5 °C min $^{-1}$. After natural cooling, a yellow solid product was collected and was ground into a fine powder for further processes.

The as-prepared g-CN (250 mg) was mixed with 5 mL of H_2SO_4 and stirred for 8 h at room temperature. After the stirring process, the mixture was slowly mixed with 50 mL of deionized (DI) water and sonicated for exfoliation. The exfoliated carbon nitride nanosheets were washed thoroughly with DI water and ethanol several times to remove residual acid. Finally, the washed light yellow solid was dried in a dry oven at 60 °C overnight.

A 50 mg amount of exfoliated carbon nitride was mixed with 10 mL of DI water and sonicated using a tip-sonicator, with a sonication power of 50 W for 5 min to form shredded and exfoliated-carbon nitride nanosheets. During the 5 min of sonication, the sample was sonicated, and rested for 5 s each, alternatingly. After sonication, the suspension of MCNs in DI water was mixed with K_2PtCl_4 solution (1.6 mg mL $^{-1}$) and stirred at 300 rpm at 70 °C for 8 h. The resulting product was washed with DI water and ethanol several times and dried in the dry oven at 60 °C overnight. The collected sample, from hence, is named Pt-MCNs.

Preparation of Pt-MCN-SnO₂ Fiber-in-Tubes. A 0.38 g amount of PVP, 0.25 g of $\text{SnCl}_2 \cdot 2\text{H}_2\text{O}$, and 15 mg of Pt-MCN were dissolved in 2 mL of DMF. The solution was stirred at room temperature for 8 h to completely dissolve PVP and $\text{SnCl}_2 \cdot 2\text{H}_2\text{O}$. Then, the solution was electrospun into nanofibers at a voltage of 15 kV and a feeding rate of 0.1 mL min $^{-1}$. A 23 gauge syringe needle was used, and the distance between the needle and collector was kept at 20 cm. Electrospun nanofibers were heat treated under air ambient at 500 °C (ramping rate 5 °C min $^{-1}$) for 1 h to form nanofibers of 15 mg of Pt-MCN-decorated tin oxide nanofiber-in-tubes (15-Pt-MCN-SnO₂ FITs). The same procedure was used to synthesize 4, 9, and 21 mg Pt-MCN-decorated and pristine tin oxide nanofiber-in-tubes (21-Pt-MCN-SnO₂, 9-Pt-MCN-SnO₂, and 4-Pt-MCN-SnO₂ FITs and pristine SnO₂ NFs), simply by altering the amount of Pt-MCNs added (Pt loading in Pt-MCN-SnO₂ varies from 0.13 wt % to 0.68 wt %). Pt precursor-added tin oxide sample (Pt-SnO₂) was synthesized by adding 1.43 mg of Pt precursor to the electrospinning solution, which is the same amount of Pt as the 15-Pt-MCN-SnO₂ FITs. MCN-added SnO₂ (MCN-SnO₂) was synthesized by adding 14.9 mg of MCNs to the electrospinning solution.

Preparation of PtNP-MCN-SnO₂ FITs. Pt nanoparticles-stabilized MCN-SnO₂ (PtNP-MCN-SnO₂) was prepared by first dispersing 14.9 mg of MCN and 671 μL of Pt nanoparticles dispersion solution in 5 mL of DI water. The mixture was stirred for 8 h at room temperature to ensure Pt nanoparticles are well stabilized on MCNs, and then the DI water was evaporated to obtain dry Pt nanoparticle-stabilized MCN (PtNP-MCN). After drying, PtNP-MCNs were redispersed in 2 mL of DMF, and 0.38 g of PVP and 0.25 g of $\text{SnCl}_2 \cdot 2\text{H}_2\text{O}$ were added and stirred to synthesize the electrospinning solution. Electrospinning and calcination processes identical to the preparation of Pt-MCN-SnO₂ were carried out to obtain PtNP-MCN-SnO₂ FITs.

Material Characterization. SEM images (FEI Magellan 400) were obtained with beam energies of 5 kV. XPS (Sigma Probe, Thermo VG Scientific) was carried out using Al $\text{K}\alpha$ radiation. All of

the XPS data obtained were calibrated with the carbon 1s peak at 284.8 eV (C–C bond). TEM characterizations were carried out using a FEI Titan cubed G2 60-300 operated at 300 kV. XRD measurements (D/MAX-2500, Rigaku) were carried out using a high-resolution powder X-ray diffractometer with Cu $\text{K}\alpha$ radiation. XAS measurements were performed on beamline 10C at the Pohang Accelerator Laboratory (PAL, Pohang, South Korea). All XAS spectra were acquired at room temperature in fluorescence mode using a double-crystal Si(111) monochromator. Analyses of both the near edge (in energy scale) and extended range (in R space) XAS spectra were performed using Athena software.

Preparation of Gas Sensor Samples. Each gas sensor sample was fabricated by first finely dispersing the sensor materials in ethanol at an equal and adequate concentration for all main samples and control samples. The finely dispersed solutions of ethanol and sensor materials were drop coated and dried on an alumina substrate with a printed Au electrode and a microheater at the backside. Schematic illustration of the gas-sensing substrate is illustrated in [Supplementary Figure 14](#).

Evaluation of Gas-Sensing Performance. The gas-sensing characteristics were evaluated using a homemade testing equipment. Prepared gas sensor samples were loaded on a 16-channel multiplexer (34902A, Agilent) connected to a data acquisition system (34972A, Agilent), which can record the real-time resistance of the gas sensors in 4 s intervals. The gas sensor samples were exposed to HCHO gas with a range of 5–0.05 ppm for 10 min and recovered with synthetic air for 10 min each time, at 275 °C. The concentration of HCHO gas was controlled using a mass flow controller. The response value was calculated by the ratio between the resistance of the gas sensor samples under air ambient (R_{air}) and the resistance of the gas sensor samples under gas exposure (R_{gas}), i.e., $R_{\text{air}}/R_{\text{gas}}$. Before the gas-sensing tests, all gas sensor samples were stabilized in air at 275 °C for at least 2 h.

ASSOCIATED CONTENT

SI Supporting Information

The Supporting Information is available free of charge at <https://pubs.acs.org/doi/10.1021/acsnano.0c03687>.

XRD data, TEM data, XPS data, XAFS fitting results, TGA/DSC data, SEM images, schematic illustration of nanofiber-in-tube formation, pore size distribution, schematic illustration of gas sensor substrate, operation temperature optimization for gas sensors toward HCHO gas, Pt-MCN-SnO₂ content optimization toward HCHO gas detection, humidity effects toward HCHO gas detection, Pt-nanoparticle-functionalized MCN-SnO₂, UPS data, EXAFS fitting parameters table, state-of-the-art HCHO gas sensors comparison table ([PDF](#))

AUTHOR INFORMATION

Corresponding Author

Il-Doo Kim – Department of Materials Science and Engineering, Korea Advanced Institute of Science and Technology, Yuseong-gu, Daejeon 34141, Republic of Korea; orcid.org/0000-0002-9970-2218; Email: idkim@kaist.ac.kr

Authors

Hamin Shin – Department of Materials Science and Engineering, Korea Advanced Institute of Science and Technology, Yuseong-gu, Daejeon 34141, Republic of Korea

Wan-Gil Jung – School of Materials Science and Engineering, Gwangju Institute of Science and Technology (GIST), Buk-gu, Gwangju 61005, Republic of Korea

Dong-Ha Kim – Department of Materials Science and Engineering, Korea Advanced Institute of Science and Technology, Yuseong-gu, Daejeon 34141, Republic of Korea

Ji-Soo Jang — Department of Materials Science and Engineering, Korea Advanced Institute of Science and Technology, Yuseong-gu, Daejeon 34141, Republic of Korea; orcid.org/0000-0001-6018-7231

Yoon Hwa Kim — Department of Materials Science and Engineering, Korea Advanced Institute of Science and Technology, Yuseong-gu, Daejeon 34141, Republic of Korea

Won-Tae Koo — Department of Materials Science and Engineering, Korea Advanced Institute of Science and Technology, Yuseong-gu, Daejeon 34141, Republic of Korea

Jaehyeong Bae — Department of Materials Science and Engineering, Korea Advanced Institute of Science and Technology, Yuseong-gu, Daejeon 34141, Republic of Korea

Chungseong Park — Department of Materials Science and Engineering, Korea Advanced Institute of Science and Technology, Yuseong-gu, Daejeon 34141, Republic of Korea

Su-Ho Cho — Department of Materials Science and Engineering, Korea Advanced Institute of Science and Technology, Yuseong-gu, Daejeon 34141, Republic of Korea

Bong Joong Kim — School of Materials Science and Engineering, Gwangju Institute of Science and Technology (GIST), Buk-gu, Gwangju 61005, Republic of Korea; orcid.org/0000-0002-5335-4342

Complete contact information is available at:

<https://pubs.acs.org/10.1021/acsnano.0c03687>

Notes

The authors declare no competing financial interest.

ACKNOWLEDGMENTS

This work was supported by Wearable Platform Materials Technology Center (WMC) funded by National Research Foundation of Korea (NRF) Grant of the Korean Government (MSIP) (No. 2016R1A5A1009926). This work was supported by the Nanomaterial Technology Development Program through the National Research Foundation of Korea (NRF) funded by the Ministry of Science, ICT and Future Planning (2016M3A7B4905609). This work was supported by the National Research Foundation of Korea (NRF) grant funded by the Korean government, Ministry of Science and ICT (2020R1A2C301312711). This work was supported by the Nano Convergence Foundation funded by the Ministry of Science and ICT (MSIT, Korea) & the Ministry of Trade, Industry and Energy (MOTIE, Korea) (Project Number 20000230).

REFERENCES

- (1) Wang, A.; Li, J.; Zhang, T. Heterogeneous Single-Atom Catalysis. *Nat. Rev. Chem.* **2018**, *2*, 65–81.
- (2) Zhu, Y.; Cao, T.; Cao, C.; Luo, J.; Chen, W.; Zheng, L.; Dong, J.; Zhang, J.; Han, Y.; Li, Z.; Chen, C.; Peng, Q.; Wang, D.; Li, Y. One-Pot Pyrolysis to N-Doped Graphene with High-Density Pt Single Atomic Sites as Heterogeneous Catalyst for Alkene Hydrosilylation. *ACS Catal.* **2018**, *8*, 10004–10011.
- (3) Qu, Y.; Chen, B.; Li, Z.; Duan, X.; Wang, L.; Lin, Y.; Yuan, T.; Zhou, F.; Hu, Y.; Yang, Z.; Zhao, C.; Wang, J.; Zhao, C.; Hu, Y.; Wu, G.; Zhang, Q.; Xu, Q.; Liu, B.; Gao, P.; You, R. Thermal Emitting Strategy to Synthesize Atomically Dispersed Pt Metal Sites from Bulk Pt Metal. *J. Am. Chem. Soc.* **2019**, *141*, 4505–4509.
- (4) Vilé, G.; Albani, D.; Nachtegaal, M.; Chen, Z.; Dontsova, D.; Antonietti, M.; López, N.; Pérez-Ramírez, J. A Stable Single-Site Palladium Catalyst for Hydrogenations. *Angew. Chem., Int. Ed.* **2015**, *54*, 11265–11269.

(5) Li, X.; Bi, W.; Zhang, L.; Shi, T.; Chu, W.; Zhang, Q.; Luo, Y.; Wu, C.; Xie, Y. Single-Atom Pt as Co-Catalyst for Enhanced Photocatalytic H₂ Evolution. *Adv. Mater.* **2016**, *28*, 2427–2431.

(6) Gao, G.; Jiao, Y.; Waclawik, E. R.; Du, A. Single Atom (Pd/Pt) Supported on Graphitic Carbon Nitride as an Efficient Photocatalyst for Visible-Light Reduction of Carbon Dioxide. *J. Am. Chem. Soc.* **2016**, *138*, 6292–6297.

(7) Liu, D.; Li, X.; Chen, S.; Yan, H.; Wang, C.; Wu, C.; Haleem, Y. A.; Duan, S.; Lu, J.; Ge, B.; Ajayan, P. M.; Luo, Y.; Jiang, J.; Song, L. Atomically Dispersed Platinum Supported on Curved Carbon Supports for Efficient Electrocatalytic Hydrogen Evolution. *Nat. Energy* **2019**, *4*, 512–518.

(8) Yao, Y.; Huang, Z.; Xie, P.; Wu, L.; Ma, L.; Li, T.; Pang, Z.; Jiao, M.; Liang, Z.; Gao, J.; He, Y.; Kline, D. J.; Zachariah, M. R.; Wang, C.; Lu, J.; Wu, T.; Li, T.; Wang, C.; Shahbazian-Yassar, R.; Hu, L. High Temperature Shockwave Stabilized Single Atoms. *Nat. Nanotechnol.* **2019**, *14*, 851–857.

(9) Zhang, S.; Nguyen, L.; Liang, J.; Shan, J.; Liu, J.; Frenkel, A. I.; Patlolla, A.; Huang, W.; Li, J.; Tao, F. Catalysis on Singly Dispersed Bimetallic Sites. *Nat. Commun.* **2015**, *6*, 1–10.

(10) Xing, F.; Jeon, J.; Toyao, T.; Shimizu, K. I.; Furukawa, S. A Cu-Pd Single-Atom Alloy Catalyst for Highly Efficient NO Reduction. *Chem. Sci.* **2019**, *10*, 8292–8298.

(11) Zhang, L.; Liu, H.; Liu, S.; Banis, M. N.; Song, Z.; Li, J.; Yang, L.; Markiewicz, M.; Zhao, Y.; Li, R.; Zheng, M.; Ye, S.; Zhao, Z.; Botton, G. A.; Sun, X. Pt/Pd Single-Atom Alloys as Highly Active Electrochemical Catalysts and the Origin of Enhanced Activity. *ACS Catal.* **2019**, *9*, 9350–9358.

(12) Zhang, X.; Cui, G.; Feng, H.; Chen, L.; Wang, H.; Wang, B.; Zhang, X.; Zheng, L.; Hong, S.; Wei, M. Platinum-Copper Single Atom Alloy Catalysts with High Performance towards Glycerol Hydrogenolysis. *Nat. Commun.* **2019**, *10*, 1–12.

(13) Greiner, M. T.; Jones, T. E.; Beeg, S.; Zwiener, L.; Scherzer, M.; Girmsdies, F.; Piccinin, S.; Armbrüster, M.; Knop-Gericke, A.; Schlögl, R. Free-Atom-Like d States in Single-Atom Alloy Catalysts. *Nat. Chem.* **2018**, *10*, 1008–1015.

(14) Giannakakis, G.; Flytzani-Stephanopoulos, M.; Sykes, E. C. H. Single-Atom Alloys as a Reductionist Approach to the Rational Design of Heterogeneous Catalysts. *Acc. Chem. Res.* **2019**, *52*, 237–247.

(15) Ren, Y.; Tang, Y.; Zhang, L.; Liu, X.; Li, L.; Miao, S.; Su, D. S.; Wang, A.; Li, J.; Zhang, T. Unraveling the Coordination Structure-Performance Relationship in Pt₁/Fe₂O₃ Single-Atom Catalyst. *Nat. Commun.* **2019**, *10*, 4500.

(16) Yoo, M.; Yu, Y.; Ha, H.; Lee, S.; Choi, J.; Oh, S.; Kang, E.; Choi, H.; An, H.; Lee, K.; Park, J. Y.; Celestre, R.; Marcus, M. A.; Nowrouzi, K.; Taube, D.; Shapiro, D.; Jung, W.; Kim, C.; Kim, H. Y. A Tailored Oxide Interface Creates Dense Pt Single-Atom Catalysts with High Catalytic Activity. *Energy Environ. Sci.* **2020**, *13*, 1231–1239.

(17) Nie, L.; Mei, D.; Xiong, H.; Peng, B.; Ren, Z.; Hernandez, X. I. P.; DeLaRiva, A.; Wang, M.; Engelhard, M. H.; Kovarik, L.; Datye, A. K.; Wang, Y. Activation of Surface Lattice Oxygen in Single-Atom Pt/CeO₂ for Low-Temperature CO Oxidation. *Science* **2017**, *358*, 1419–1423.

(18) Lee, B.-H.; Park, S.; Kim, M.; Sinha, A. K.; Lee, S. C.; Jung, E.; Chang, W. J.; Le, K.; Kim, J. H.; Cho, S.; Kim, H.; Nam, K. T.; Hyeon, T. Reversible and Cooperative Photoactivation of Single-Atom Cu/TiO₂ hotocatalysts. *Nat. Mater.* **2019**, *18*, 620–626.

(19) Qiao, B.; Wang, A.; Yang, X.; Allard, L. F.; Jiang, Z.; Cui, Y.; Liu, J.; Li, J.; Zhang, T. Single-Atom Catalysis of CO Oxidation Using Pt₁/FeO_x. *Nat. Chem.* **2011**, *3*, 634–641.

(20) Jones, J.; Xiong, H.; DelaRiva, A. T.; Peterson, E. J.; Phan, H.; Challa, S. R.; Qi, G.; Oh, S.; Wiebenga, M. H.; Hernández, X. I. P.; Wang, Y.; Datye, A. K. Thermally Stable Single-Atom Platinum-On-Ceria Catalysts via Atom Trapping. *Science* **2016**, *353*, 150–154.

(21) Lin, J.; Qiao, B.; Li, N.; Li, L.; Sun, X.; Liu, J.; Wang, X.; Zhang, T. Little Do More: A Highly Effective Pt₁/FeO_x Single-Atom Catalyst

- for the Reduction of NO by H₂. *Chem. Commun.* **2015**, *51*, 7911–7914.
- (22) Xin, P.; Li, J.; Xiong, Y.; Wu, X.; Dong, J.; Chen, W.; Wang, Y.; Gu, L.; Luo, J.; Rong, H.; Chen, C.; Peng, Q.; Wang, D.; Li, Y. Revealing the Active Species for Aerobic Alcohol Oxidation by Using Uniform Supported Palladium Catalysts. *Angew. Chem.* **2018**, *130*, 4732–4736.
- (23) Hu, M.; Zhang, J.; Zhu, W.; Chen, Z.; Gao, X.; Du, X.; Wan, J.; Zhou, K.; Chen, C.; Li, Y. 50 ppm of Pd Dispersed on Ni(OH)₂ Nanosheets Catalyzing Semi-Hydrogenation of Acetylene with High Activity and Selectivity. *Nano Res.* **2018**, *11*, 905–912.
- (24) Wan, J.; Chen, W.; Jia, C.; Zheng, L.; Dong, J.; Zheng, X.; Wang, Y.; Yan, W.; Chen, C.; Peng, Q.; Wang, D.; Li, Y. Defect Effects on TiO₂ Nanosheets: Stabilizing Single Atomic Site Au and Promoting Catalytic Properties. *Adv. Mater.* **2018**, *30*, 1705369.
- (25) Zhang, J.; Wu, X.; Cheong, W.; Chen, W.; Lin, R.; Li, J.; Zheng, L.; Yan, W.; Gu, L.; Chen, C.; Peng, Q.; Wang, D.; Li, Y. Cation Vacancy Stabilization of Single-Atomic-Site Pt₁/Ni(OH)_x Catalyst for Diboration of Alkynes and Alkenes. *Nat. Commun.* **2018**, *9*, 1002.
- (26) Kyriakou, G.; Boucher, M. B.; Jewell, A. D.; Lewis, E. A.; Lawton, T. J.; Baber, A. E.; Tierney, H. L.; Flytzani-Stephanopoulos, M.; Sykes, E. C. H. Isolated Metal Atom Geometries as a Strategy for Selective Heterogeneous Hydrogenations. *Science* **2012**, *335*, 1209–1212.
- (27) Zaera, F. Nanostructured Materials for Applications in Heterogeneous Catalysis. *Chem. Soc. Rev.* **2013**, *42*, 2746–2762.
- (28) Prieto, G.; Tuysuz, H.; Duyckaerts, N.; Knossalla, J.; Wang, G.; Schüth, F. Hollow Nano- and Microstructures as Catalysts. *Chem. Rev.* **2016**, *116*, 14056–14119.
- (29) Munnik, P.; De Jongh, P. E.; De Jong, K. P. Recent Developments in the Synthesis of Supported Catalysts. *Chem. Rev.* **2015**, *115*, 6687–6718.
- (30) DeRita, L.; Dai, S.; Lopez-Zepeda, K.; Pham, N.; Graham, G. W.; Pan, X.; Christopher, P. Catalyst Architecture for Stable Single Atom Dispersion Enables Site-Specific Spectroscopic and Reactivity Measurements of CO Adsorbed to Pt Atoms, Oxidized Pt Clusters, and Metallic Pt Clusters on TiO₂. *J. Am. Chem. Soc.* **2017**, *139*, 14150–14165.
- (31) Shan, J.; Li, M.; Allard, L. F.; Lee, S.; Flytzani-Stephanopoulos, M. Mild Oxidation of Methane to Methanol or Acetic Acid on Supported Isolated Rhodium Catalysts. *Nature* **2017**, *551*, 605–608.
- (32) Liu, P.; Zhao, Y.; Qin, R.; Mo, S.; Chen, G.; Gu, L.; Chevrier, D. M.; Zhang, P.; Guo, Q.; Zang, D.; Wu, B.; Fu, G.; Zheng, N. Catalysis: Photochemical Route for Synthesizing Atomically Dispersed Palladium Catalysts. *Science* **2016**, *352*, 797–800.
- (33) Wang, Y.; Wang, X.; Antonietti, M. Polymeric Graphitic Carbon Nitride as a Heterogeneous Organocatalyst: From Photochemistry to Multipurpose Catalysis to Sustainable Chemistry. *Angew. Chem., Int. Ed.* **2012**, *51*, 68–89.
- (34) Li, Q.; He, Y.; Peng, R. One-Step Synthesis of SnO₂ Nanoparticles-Loaded Graphitic Carbon Nitride and Their Application in Thermal Decomposition of Ammonium Perchlorate. *New J. Chem.* **2015**, *39*, 8703–8707.
- (35) An, X.; Hu, C.; Lan, H.; Liu, H.; Qu, J. Strongly Coupled Metal Oxide/Reassembled Carbon Nitride/Co-Pt Heterostructures for Efficient Photoelectrochemical Water Splitting. *ACS Appl. Mater. Interfaces* **2018**, *10*, 6424–6432.
- (36) Yousaf, M. U.; Pervaiz, E.; Minallah, S.; Afzal, M. J.; Honghong, L.; Yang, M. Tin Oxide Quantum Dots Decorated Graphitic Carbon Nitride for Enhanced Removal of Organic Components from Water: Green Process. *Results Phys.* **2019**, *14*, 102455.
- (37) He, C.; Zhang, J. H.; Zhang, W. X.; Li, T. T. Type-II InSe/g-C₃N₄ Heterostructure as a High-Efficiency Oxygen Evolution Reaction Catalyst for Photoelectrochemical Water Splitting. *J. Phys. Chem. Lett.* **2019**, *10*, 3122–3128.
- (38) Xu, J.; Zhang, L.; Shi, R.; Zhu, Y. Chemical Exfoliation of Graphitic Carbon Nitride for Efficient Heterogeneous Photocatalysis. *J. Mater. Chem. A* **2013**, *1*, 14766–14772.
- (39) Liu, L.; Wu, X.; Wang, L.; Xu, X.; Gan, L.; Si, Z.; Li, J.; Zhang, Q.; Liu, Y.; Zhao, Y.; Ran, R.; Wu, X.; Weng, D.; Kang, F. Atomic Palladium on Graphitic Carbon Nitride as a Hydrogen Evolution Catalyst under Visible Light Irradiation. *Commun. Chem.* **2019**, *2*, 18.
- (40) Jang, J. S.; Yu, S.; Choi, S. J.; Kim, S. J.; Koo, W. T.; Kim, I. D. Metal Chelation Assisted *In Situ* Migration and Functionalization of Catalysts on Peapod-Like Hollow SnO₂ toward a Superior Chemical Sensor. *Small* **2016**, *12*, 5989–5997.
- (41) Oh, S.; Back, S.; Doh, W. H.; Moon, S. Y.; Kim, J.; Jung, Y.; Park, J. Y. Probing Surface Oxide Formations on SiO₂-Supported Platinum Nanocatalysts Under CO Oxidation. *RSC Adv.* **2017**, *7*, 45003–45009.
- (42) Guilera, G.; Newton, M. A.; Polli, C.; Pascarelli, S.; Guinó, M.; Hii, K. K. *In Situ* Investigation of the Oxidative Addition in Homogeneous Pd Catalysts by Synchronised Time Resolved UV-Vis/EXAFS. *Chem. Commun.* **2006**, 4306–4308.
- (43) Alayoglu, S.; Zavalij, P.; Eichhorn, B.; Wang, Q.; Frenkel, A. I.; Chupas, P. Structural and Architectural Evaluation of Bimetallic Nanoparticles: A Case Study of Pt-Ru Core-Shell and Alloy Nanoparticles. *ACS Nano* **2009**, *3*, 3127–3137.
- (44) Sano, T.; Tsutsui, S.; Koike, K.; Hirakawa, T.; Teramoto, Y.; Negishi, N.; Takeuchi, K. Activation of Graphitic Carbon Nitride (g-C₃N₄) by Alkaline Hydrothermal Treatment for Photocatalytic NO Oxidation in Gas Phase. *J. Mater. Chem. A* **2013**, *1*, 6489–6496.
- (45) Cui, Y.; Zhang, J.; Zhang, G.; Huang, J.; Liu, P.; Antonietti, M.; Wang, X. Synthesis of Bulk and Nanoporous Carbon Nitride Polymers from Ammonium Thiocyanate for Photocatalytic Hydrogen Evolution. *J. Mater. Chem.* **2011**, *21*, 13032–13039.
- (46) Wang, D.; Huang, S.; Li, H.; Chen, A.; Wang, P.; Yang, J.; Wang, X.; Yang, J. Ultrathin WO₃ Nanosheets Modified by g-C₃N₄ for Highly Efficient Acetone Vapor Detection. *Sens. Actuators, B* **2019**, *282*, 961–971.
- (47) Cui, L.; Liu, Y.; Fang, X.; Yin, C.; Li, S.; Sun, D.; Kang, S. Scalable and Clean Exfoliation of Graphitic Carbon Nitride in NaClO Solution: Enriched Surface Active Sites for Enhanced Photocatalytic H₂ Evolution. *Green Chem.* **2018**, *20*, 1354–1361.
- (48) Cao, S.; Low, J.; Yu, J.; Jaroniec, M. Polymeric Photocatalysts Based on Graphitic Carbon Nitride. *Adv. Mater.* **2015**, *27*, 2150–2176.
- (49) Zhou, Z.; Zhang, Y.; Shen, Y.; Liu, S.; Zhang, Y. Molecular Engineering of Polymeric Carbon Nitride: Advancing Applications from Photocatalysis to Biosensing and More. *Chem. Soc. Rev.* **2018**, *47*, 2298–2321.
- (50) Zhang, Y.; Liu, J.; Wu, G.; Chen, W. Porous Graphitic Carbon Nitride Synthesized via Direct Polymerization of Urea for Efficient Sunlight-Driven Photocatalytic Hydrogen Production. *Nanoscale* **2012**, *4*, 5300–5303.
- (51) Zhang, S.; Hang, N.; Zhang, Z.; Yue, H.; Yang, W. Preparation of g-C₃N₄/Graphene Composite for Detecting NO₂ at Room Temperature. *Nanomaterials* **2017**, *7*, 12.
- (52) Jeong, Y. J.; Kim, D.; Jang, J.; Kang, J.; Kim, R.; Kim, I. Bio-Inspired Heterogeneous Sensitization of Bimetal Oxides on SnO₂ Scaffolds for Unparalleled Formaldehyde Detection. *Chem. Commun.* **2019**, *55*, 3622–3625.
- (53) Kang, J. Y.; Jang, J.; Koo, W.; Seo, J.; Choi, Y.; Kim, M.; Kim, D.; Cho, H.; Jung, W.; Kim, I. Perovskite La_{0.75}Sr_{0.25}Cr_{0.5}Mn_{0.5}O_{3-δ} Sensitized SnO₂ Fiber-In-Tube Scaffold: Highly Selective and Sensitive Formaldehyde Sensing. *J. Mater. Chem. A* **2018**, *6*, 10543–10551.
- (54) Kim, R. H.; Jang, J. S.; Kim, D. H.; Kang, J. Y.; Cho, H. J.; Jeong, Y. J.; Kim, I. D. A General Synthesis of Crumpled Metal Oxide Nanosheets as Superior Chemiresistive Sensing Layers. *Adv. Funct. Mater.* **2019**, *29*, 1903128.
- (55) Kim, D. H.; Jang, J. S.; Koo, W. T.; Kim, I. D. Graphene Oxide Templating: Facile Synthesis of Morphology Engineered Crumpled SnO₂ Nanofibers for Superior Chemiresistors. *J. Mater. Chem. A* **2018**, *6*, 13825–13834.
- (56) Bulemo, P. M.; Cho, H. J.; Kim, D. H.; Kim, I. D. Facile Synthesis of Pt-Functionalized Meso/Macroporous SnO₂ Hollow

Spheres through *In Situ* Templating with SiO₂ for H₂S Sensors. *ACS Appl. Mater. Interfaces* **2018**, *10*, 18183–18191.

(57) Kim, S. J.; Choi, S. J.; Jang, J. S.; Cho, H. J.; Koo, W. T.; Tuller, H. L.; Kim, I. D. Exceptional High-Performance of Pt-Based Bimetallic Catalysts for Exclusive Detection of Exhaled Biomarkers. *Adv. Mater.* **2017**, *29*, 1700737.

(58) Kim, S. J.; Choi, S. J.; Jang, J. S.; Kim, N. H.; Hakim, M.; Tuller, H. L.; Kim, I. D. Mesoporous WO₃ Nanofibers with Protein-Templated Nanoscale Catalysts for Detection of Trace Biomarkers in Exhaled Breath. *ACS Nano* **2016**, *10*, 5891–5899.

(59) Hu, H.; Zhu, J.; Yang, F.; Chen, Z.; Deng, M.; Weng, L.; Ling, Y.; Zhou, Y. A Robust: *etb*-Type Metal-Organic Framework Showing Polarity-Exclusive Adsorption of Acetone over Methanol for Their Azeotropic Mixture. *Chem. Commun.* **2019**, *55*, 6495–6498.

(60) Jang, J. S.; Kim, S. J.; Choi, S. J.; Kim, N. H.; Hakim, M.; Rothschild, A.; Kim, I. D. Thin-Walled SnO₂ Nanotubes Functionalized with Pt and Au Catalysts *via* the Protein Templating Route and Their Selective Detection of Acetone and Hydrogen Sulfide Molecules. *Nanoscale* **2015**, *7*, 16417–16426.

(61) Degler, D.; Carvalho, H. W. P.; Kvashnina, K.; Grunwaldt, J. D.; Weimar, U.; Barsan, N. Structure and Chemistry of Surface-Doped Pt:SnO₂ Gas Sensing Materials. *RSC Adv.* **2016**, *6*, 28149–28155.

(62) Großmann, K.; Wicker, S.; Weimar, U.; Barsan, N. Impact of Pt Additives on the Surface Reactions Between SnO₂, Water Vapour, CO and H₂; An Operando Investigation. *Phys. Chem. Chem. Phys.* **2013**, *15*, 19151–19158.

(63) Jang, J. S.; Lim, Y. W.; Kim, D. H.; Lee, D.; Koo, W. T.; Lee, H.; Bae, B. S.; Kim, I. D. Glass-Fabric Reinforced Ag Nanowire/Siloxane Composite Heater Substrate: Sub-10 nm Metal@Metal Oxide Nanosheet for Sensitive Flexible Sensing Platform. *Small* **2018**, *14*, 1802260.

(64) Liu, J.; Jiao, M.; Lu, L.; Barkholtz, H. M.; Li, Y.; Wang, Y.; Jiang, L.; Wu, Z.; Liu, D.; Zhuang, L.; Ma, C.; Zheng, J.; Zhang, B.; Su, D.; Song, P.; Xing, W.; Xu, W.; Wang, Y.; Jiang, Z.; Sun, G. High Performance Platinum Single Atom Electrocatalyst for Oxygen Reduction Reaction. *Nat. Commun.* **2017**, *8*, 16160.